Numerical simulation of a three-dimensional flow in a channel with interaction of a plane shock wave and a longitudinally ribbed surface

I.I. Mazhul

Khristianovich Institute of Theoretical and Applied Mechanics SB RAS, Novosibirsk, Russia

E-mail: mazhul@itam.nsc.ru

Results of numerical simulations of a supersonic flow in a channel with a rectangular cross section having a longitudinally ribbed bottom surface are reported. The channel contains a tapered inlet section, where the cowl lip generates a shock wave incident onto the bottom surface, and a posterior constant-area section. The present numerical simulations are performed for a viscous three-dimensional flow with the use of the Reynolds-averaged Navier–Stokes equations and k-ω SST turbulence model. The computations are performed for the free-stream Mach number M = 4.

Introduction

Supersonic flow deceleration in a plane intake is associated with shock wave-boundary layer interaction leading to the formation of separation regions. In particular, such interaction occurs in the intake entrance region due to incidence of a shock wave generated by the cowl onto the compression wedge surface. Prevention of boundary layer separation at the intake entrance is of large practical significance because it affects the intake operation efficiency. Various methods of boundary layer control are used to eliminate its low-energy part, which favors flow separation.

One of the effective methods of flow control and prevention of boundary layer separation is boundary layer bleeding [1, 2]. For this purpose, it is possible to use transverse bleeding slots or perforated panels at the place of shock wave incidence onto the compression wedge. A disadvantage of transverse bleeding slots is their fixed position regardless of the aircraft flight regime. To take into account the supersonic flow velocity at the entrance, it is possible to use several consecutively aligned slots of the visor-type [3]. The efficiency of using perforated panels for boundary layer bleeding was studied in [4, 5]. In particular, the data obtained in the T-313 blowdown wind tunnel based at the Khristianovich Institute of Theoretical and Applied Mechanics of the Siberian Branch of the Russian Academy of Sciences (ITAM SB RAS) in the Mach number range M = 2 – 6 and in the IT-302M hotshot wind tunnel at M = 5 – 8 showed that perforated bleeding is an effective method for intake control. Thus, at M = 4, the flow rate

coefficient was approximately 20 % higher and the total pressure loss was two times smaller than the corresponding values obtained without boundary layer bleeding.

In addition to transverse slots for boundary layer bleeding, longitudinal slots are also used. For example, authors of [6] used a convergent intake configuration to study the efficiency of streamwise slots located in the corner region along the side cheeks. The flow rate increased by $\sim 30\%$ at M = 2 and by 10–15 % at M = 4 as compared to the variant without boundary layer bleeding. A supersonic three-dimensional intake based on V-shaped bodies and equipped with rotating panels was considered in [7, 8]. When these panels were rotated, transverse and longitudinal slots were formed that ensured boundary layer bleeding or air bypassing in the course of intake starting. Experimental data obtained at M = 1.75 and 2 confirmed the operational capability of bleeding slots and intake efficiency.

In contrast to the investigations [6 – 8], author of [9] proposed to make the compression surface of a plane intake at the place of shock wave incidence in the form of a surface with spanwise-distributed longitudinally-aligned slots for boundary layer bleeding or air bypassing. It was assumed that boundary layer bleeding through longitudinal slots could be more effective than boundary layer suction through perforation holes. The slot length was to be chosen with allowance for the position of incidence of the shock wave from the lip onto the wedge compression surface of the intake depending on the flight regime. The width of the streamwise slots could be fixed or adjustable, which was provided by moving elements with a triangular cross section. Thus, there arose a question of interaction of the shock wave generated by the intake cowl lip with the boundary layer on a longitudinally-ribbed surface. There are practically no investigations of this kind.

Authors of [10] considered the use of longitudinal ribbing of the surface (riblets) for the purpose of reducing the friction in the turbulent boundary layer and delaying the laminar-turbulent transition. Authors of [11] studied a separated flow around a wing with a small aspect ratio and a streamwise-wavy surface at subsonic velocities. It was shown that surface waviness leads to a radical change in the structure of the separated flow above the wing, namely, the laminar flow separation region over the span of a smooth wing disintegrated into local separation regions in valleys between the surface waves. The change in the flow structure resulted in an increase in the critical angle of attack of the wing by a factor of 1.5. In this aspect, data on heat fluxes toward the wavy surfaces at supersonic velocities are also of interest. Such data were obtained in [12] by using temperature-sensitive paints in the case of the transverse and streamwise flow of the turbulent boundary layer past a wavy surface at M = 4. In the case of the streamwise flow, the mean level of heat transfer to the wavy surface could be smaller approximately by 20 % than that in the flat plate case. The minimum values of the heat transfer coefficient were observed in the region of the maximum depth of the wave. A similar result was obtained in [13] for the streamwise wave at the Mach number M = 10.3.

The goal of the present study was to find the flow structure in the case of shock wave interaction with a longitudinally-ribbed bottom surface in a rectangular channel of a model intake. The purpose was to study the characteristics of an innovative intake proposed in [9]. The numerical simulations of the 3D flow were performed at M = 4 with the use of the Reynolds-averaged Navier–Stokes equations and the k-ω SST turbulence model [14]. Examples of computations of separated flows with the use of various turbulence models, including the k-ω SST model, can be found in [15]. The results of the numerical simulations of the flow in the configuration of this kind with a flat bottom surface of the channel were reported in [16].

Configuration and simulation conditions

We consider a model configuration, which is the initial section of a plane intake with an internal channel having a rectangular cross section. The configuration contains a tapered input section with a compression wedge (cowl) with an angle δ_w and a throat with a constant cross section (Fig. 1). The compression wedge generates a shock wave, which interacts with

the boundary layer on the inner walls of the channel. The size of the model configuration and the simulation conditions were chosen on the basis of requirements of model testing in the wind tunnel T-313 ITAM SB RAS at the Mach number M = 4.

The height of the air intake $H_0 = 0.04$ m. The flat plate with a length of $L_0 = 0.29$ m was mounted in front of the intake. This allowed modeling the boundary layer growth before entering the air intake. The compression wedge had an angle $\delta_w = 10°$, and the intensity of the shock wave formed at M = 4 was sufficient for boundary layer separation from the longitudinally-ribbed bottom surface of the channel. The relative throat area was $H_{th}/H_0 = 0.58$, the relative width of the intake in the throat cross section was $B/H_{th} = 3.19$, and the relative length of the throat section was $L_{th}/H_{th} = 2.8$. The intake width was $B = 0.075$ m.

The bottom surface of the rectangular channel was equipped with longitudinally-aligned ribs having a triangular cross section. The height and width of the rib base were 5 mm, and the distance between the rib tips was 10 mm. Longitudinal valleys 5 mm wide were formed between the ribs. In the coordinate system used, the vertical plane of symmetry of the configuration corresponded to the coordinate $z = 0$ and passed through the rib tip.

The data were computed for a viscous flow around this configuration by means of solving the Reynolds-averaged Navier–Stokes equations with the use of the k-ω SST turbulence model. All computations were performed with the use of the Fluent software [14] and an explicit second-order upwind scheme. The problem was solved in two stages. At the first stage, the turbulent boundary layer on the nose plate was calculated, i.e., the velocity profile and other flow parameters in the intake entrance cross section were determined (the velocity profile in the intake entrance cross section is compared in Fig. 5 with the velocity profile in the case of development of the boundary layer on the bottom surface of the configuration; the boundary layer thickness in the intake entrance cross section is $\delta_{b.l.} \approx 4.5$ mm). The results were used at the second stage for calculating the flow in the channel.

The computational grid was refined toward the side walls of the channel and near the ribs and valleys between them, which ensured the values $y^+ < 1$ both on the wide walls and on the longitudinal ribs. The grid in the boundary layer ahead of the separation region contained approximately 50 cells. In the computational domain (from the intake entrance to exit cross section), the computational grid had approximately $17 \cdot 10^6$ nodes. For studying the grid convergence, several grids were considered: those with $17 \cdot 10^6$, $20.4 \cdot 10^6$, and $22.6 \cdot 10^6$ nodes. The number of nodes was increased by adapting the grid on the bottom surface of the configuration, which was expected to reveal a certain effect in the case of shock wave-boundary layer interaction on this surface. The flow rate coefficient (ratio of the air flow rate in the exit cross section to the flow rate in the entrance cross section) was used as a parameter determining the grid convergence. The computations on different grids showed that the difference in the flow rate coefficient is within $\sim 0.07\%$, which is fairly admissible for practical applications. It should be noted that the flow symmetry conditions were not imposed though the configuration has a vertical plane of symmetry.

The input boundary of the computational domain coincided with the channel entrance cross section. The conditions imposed here were the flow parameters obtained in the nose
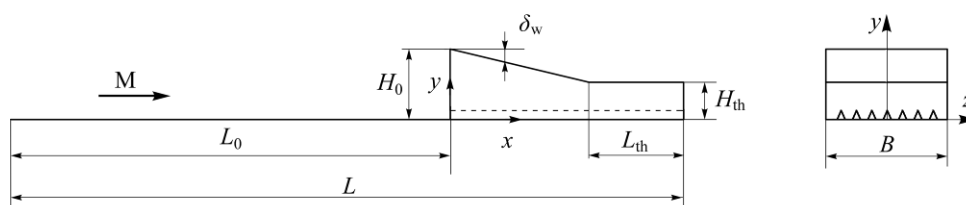

Fig. 1. Scheme of the model configuration and coordinate system.

plate computations performed at the first stage. The initial parameters inside the computational domain corresponded to the flow parameters at the entrance, while the parameters in the channel exit cross section corresponded to the static pressure and stagnation temperature in the free stream. The no-slip condition was applied at the channel walls, which were assumed to be adiabatic. Stabilization of a steady flow in the numerical solution of the problem was controlled by reaching identical air flow rates in the entrance and exit cross sections of the channel. In the computations reported here, the difference was within 0.06 %. The data were computed for the free-stream Mach number $M = 4$, stagnation pressure $P_0 = 10.3$ bar, stagnation temperature $T_0 = 290$ K, and unit Reynolds number $Re_1 = 48 \cdot 10^6$ 1/m.

Flow in the intake channel

In the case of a viscous flow in the inner channel with a triangular cross section of the configuration under study with a longitudinally-ribbed bottom surface, the governing factor is interaction of the shock wave induced by the compression wedge of the intake with the boundary layer on the channel surfaces.

The flow structure directly on the channel walls can be estimated by considering Fig. 2, which shows the streamlines of the viscous flow on the surface constructed on the basis of the components τ_x, τ_y, and τ_z of the skin friction. The figure also shows the horizontal lines y_1, y_2, and y_3 with the normalized coordinates $y = y/H_{th} = 0.19$, 0.43, and 0.85, respectively, on which the pressure distributions are further presented. The line z_0 is the plane of symmetry of the configuration.
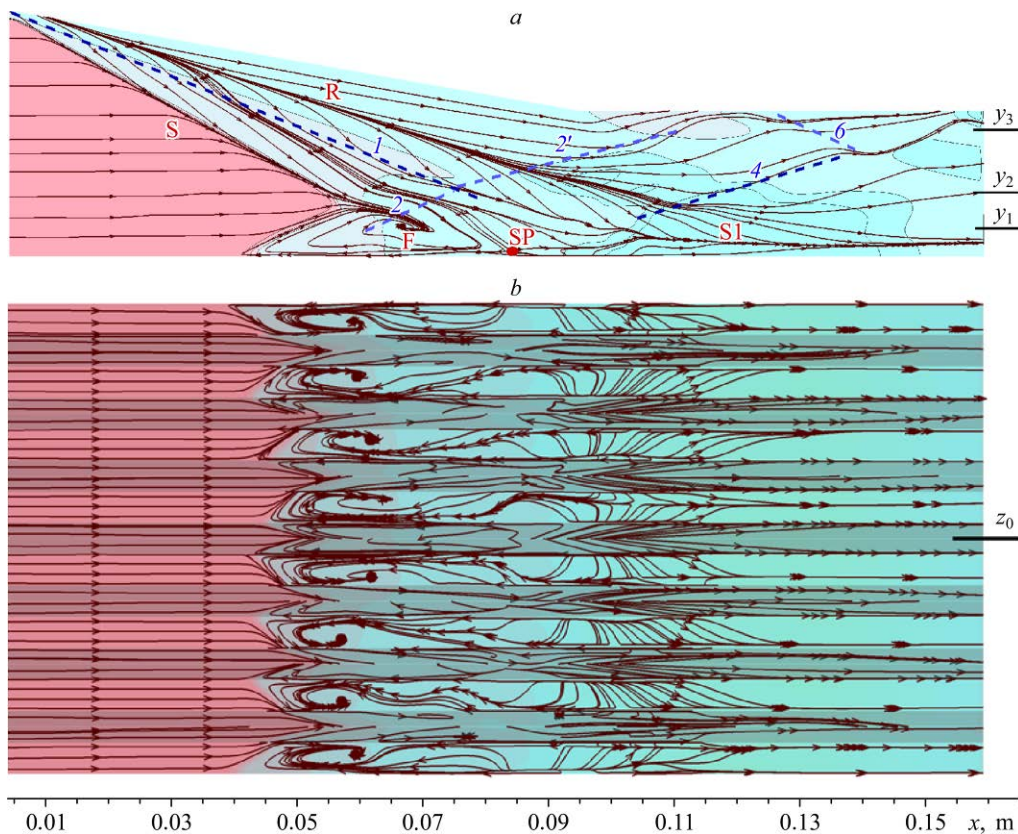

Fig. 2. Limiting streamlines on the side (*a*) and bottom (*b*) surfaces.
z_0 — plane of symmetry.

The streamlines of the viscous flow on the surface can be interpreted as the limiting streamlines, which allows one to estimate the flow direction near the surface. It should be noted that the transverse flow pattern on the ribbed bottom surface is almost symmetric with respect to the vertical plane of symmetry (Fig. 2*b*). The boundary layer separation lines in the region $x \sim 0.04 - 0.05$ m are swept both on the ribs proper and in the valleys between them.

The boundary layer separation region on the side surface (Fig. 2*a*) is determined by the positions of the separation line S and reattachment line R. The separation starts under the action of the shock wave *1* from the compression wedge and separation shock *2* shown further in Fig. 4*a*. These shock waves are responsible for the complicated shape of the separation line S. Thus, the flow behind the shock wave *1* from the compression wedge is characterized by the predominant direction of the flow toward the bottom surface with the velocity component $V_y < 0$. The flow behind the separation shock *2*, vice versa, is directed away from the bottom surface, and $V_y > 0$. This will be further seen in Fig. 4*b* as different directions of the streamlines in the flow structure. As was noted in experimental investigations of the flow in half-channels [17], interaction of differently directed flows leads to the formation of a focus F. Behind the separation region, one can see the formation of the separation line S1 emanating from the saddle point SP, which indicates the possibility of the formation of streamwise vortex structures.

More details of the flow on the ribbed bottom surface near the vertical plane of symmetry can be obtained from Fig. 3. The flow domain is bounded by the boundary layer separation region at $x \sim 0.035 - 0.115$ m in the longitudinal direction and by the rib and the neighboring valleys in the transverse direction. Here curves *1* and *1'* are the faces of the longitudinal rib; curves *2* and *2'* are the horizontal surfaces (valleys) between the ribs; finally, curves *3* and *4* are the separation lines on the horizontal surfaces and on the ribs, respectively; curves *A-A* and *B-B* indicate the side boundaries of the valley. The divergence of the surface streamlines also allows one to see the reattachment regions *5* on the ribs and valleys at $x \sim 0.09 - 0.1$ m. The flow reattachment region *5* is followed by the longitudinal separation and reattachment lines emanating from the saddle point SP and node point N, respectively. The scale of flow presentation does not allow a detailed topological analysis of singular points; only some positions of the foci F, saddle points SP, and node points N are indicated here.

The swept character (certain slope with respect to the longitudinal axis of the configuration) of the boundary layer separation lines in the valleys between the ribs can be probably associated with the presence of the foci F and opposite directions of the limiting streamlines (i.e., of the flow velocity) near the side boundaries *A-A* and *B-B* of the valley. These factors provide different effects on the near-wall flow in the separation region and, as a consequence, different positions of the boundary layer separation beginning. The analysis of numerical data shows that the dynamic pressures in the near-wall part of the boundary layer are lower in the vicinity of the separation line *3* adjacent to the rib *A-A*, which favors earlier separation. Here one can also see lower values of the skin friction components τ_x than those observed in a similar region near the rib *B-B*. The swept character of the separation lines on the longitudinal rib is associated with the incidence of an oblique separation shock *2* onto this rib (see Fig. 4).
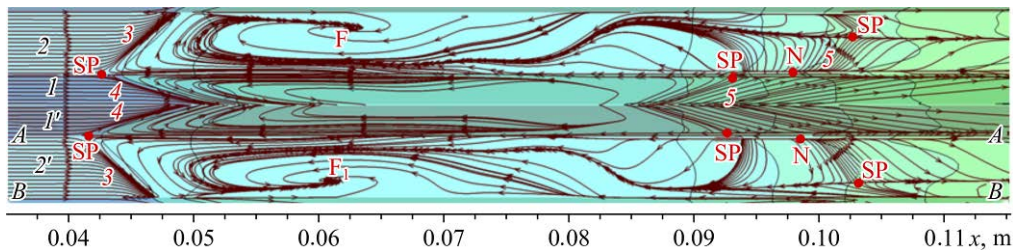

Fig. 3. Limiting streamlines in the longitudinal rib region.

The flow patterns in the vertical plane of symmetry of the configuration ($z = 0$) and in the longitudinal cross section $z = 0.005$ m (middle of the nearby valley) are illustrated in Fig. 4, which shows the Mach number contours and streamlines constructed on the basis of the velocity components V_x and V_y. The incidence of the shock wave *1* from the compression wedge onto the bottom surface induces boundary layer separation and, as a consequence, the formation of the separation shock wave *2*. Their interaction leads to the formation of the shock waves *1′* and *2′*. It should be noted that it is the separation shock *2* that is responsible for flow separation on the longitudinal ribs. Behind the boundary layer separation region, there is a hanging reattachment shock *4*, the shock wave reflected from the upper surface *6*, and the results of their intersection: shock waves *4′* and *6′*. One can also see the expansion fan *3* above the separation region and the expansion fan *5* at the corner point of the upper contour of the channel. It follows from the distributions of the streamlines of the longitudinal flow that the flow behind the separation region and behind the reattachment shock *4* is mainly directed upward from the bottom surface.

From the distribution of the streamlines in Fig. 4*b*, one can see that the boundary layer separation region in the cross section under consideration is located in the interval $x \sim 0.043$–0.096 m. This fact is consistent with the positions of the separation line and reattachment line on the surface presented earlier in Fig. 3. The separation and reattachment lines both on the valleys and on the faces of the longitudinal ribs have a swept character. Moreover, it should be noted that swept separation of the boundary layer (region $x = 0.042$–0.047 m) on the horizontal surfaces of the valleys occurs earlier than that in the flow on a flat bottom surface ($x \sim 0.07$ m, plane of symmetry); the data for the latter situation were obtained in [16] for similar initial conditions of the flow. Apparently, this is related to the formation of the initial zone of the separated flow induced by the presence of the foci F (see Fig. 3, the foci are located at $x \sim 0.062$ m). Upstream shifting of the separation lines as compared to the flow in an open dihedral corner and on a flat plate was also observed in the experimental studies of the flow in a rectangular half-channel [17, 18].

Let us consider the profiles of the streamwise velocity component V_x in the section $z = 0.005$ m (middle of the valley); the general structure of the flow in this section is shown in Fig. 4*b*. These data in the boundary layer region are shown in Fig. 5*a* in several characteristic
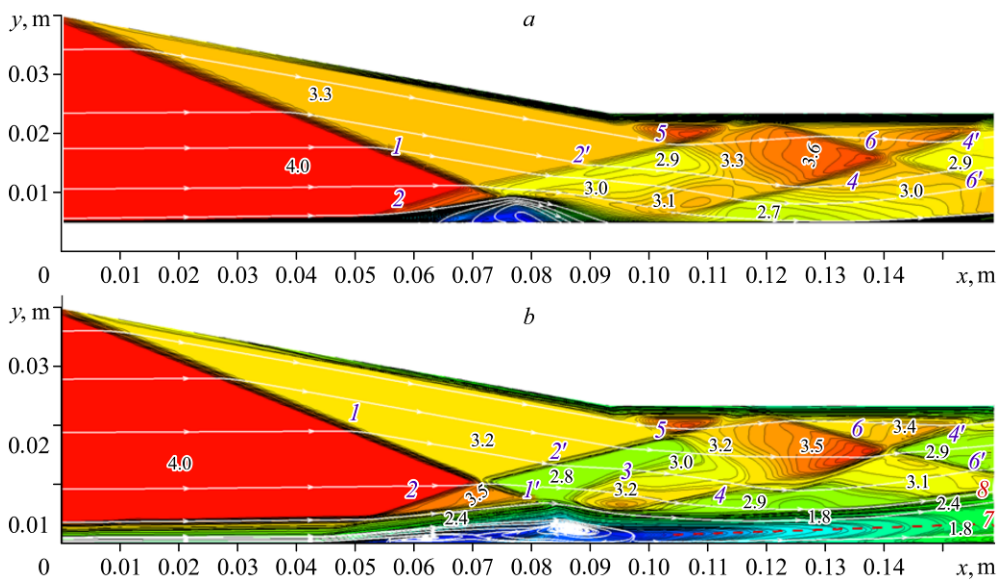

Fig. 4. Flow structure in the plane of symmetry $z = 0$ (*a*) and in the cross section $z = 0.005$ m (*b*).

cross sections $x = \text{const}$: $\overline{V}_x = V_x / V_{\text{fs}}$, where V_{fs} is the velocity of the freestream flow. For comparison, the figure also shows the velocity profiles ahead of the boundary layer separation region at $x = 0.04$ m (curve *1*) and the initial profile in the intake entrance cross section at $x = 0$ (curve *8*). The boundary layer thickness ahead of the separation region is comparable with the height of the longitudinal ribs: $\sim 4.7 - 5$ mm. Directly in the separation region $V_x < 0$ (curve *2*), and the separation region (recirculation region) the height determined from the reattachment streamline (see Fig. 4*b*) is approximately 4 mm. Using the data of Fig. 5, the boundary layer thickness can be estimated by the transition of the profile $\overline{V}_x(y)$ to the vertical branch. The separated boundary layer flows around the recirculation region, and its height in the cross section $x = 0.085$ m reaches approximately 7 mm. After boundary layer reattachment ($x > 0.1$ m), the boundary layer flow is accelerated and its thickness increases. The profile of the longitudinal velocity component has a typical S-shaped form with a "maximum" in the near-wall part of the boundary layer and a "minimum" at a certain distance from it. The approximate position of this "minimum" determined from the numerical data is denoted in Fig. 4*b* by curve *7*.

The specific features of the longitudinal velocity profile correspond to the total pressure losses of the flow shown in Fig. 5*b*. Here $\sigma = P_0 / P_{0\text{fs}}$ is the total pressure loss coefficient, and $P_{0\text{fs}}$ is the total pressure in the freestream flow. It is seen from the profiles in Fig. 5 that a new near-wall boundary layer starts to develop behind the separation region, where the total pressure loss decreases over the height owing to reduction of viscous effects, i.e., the value of σ increases. At the same time, the separated boundary layer flowing around the separation region, where the total pressure loss is high, arrives in this region. For example, the total pressure loss in the cross section $x = 0.085$ m directly above the separation region corresponds to $\sigma \sim 0.02 \div 0.03$. Additional losses over the height of this layer are also observed downstream, when passing through compression waves forming further the reattachment shock *4*. Thus, the flow with sufficiently high pressure losses enters the region of the reattached boundary layer, resulting in an S-shaped form of the profile $\sigma(y)$ with a local maximum near the wall and a local minimum at a certain distance from the wall. The positions of this minimum over the height coincide for the profiles $\sigma(y)$ and $\overline{V}_x(y)$. As was already noted, the approximate position of this minimum in Fig. 4*b* is denoted by curve *7*. The increase in the values of $\sigma(y)$ after this minimum is caused by reduction of the total pressure loss in the separated boundary layer with increasing vertical coordinate.

The distributions of the relative pressure along the bottom surface are shown in Fig. 6 in two longitudinal sections: along the rib at $z = 0$ and along the middle of the valley at $z = 0.005$ m. It is seen that the boundary layer starts to separate in the region $x \sim 0.04 \div 0.045$ m, which is consistent with the distributions of the separation lines in Fig. 3.
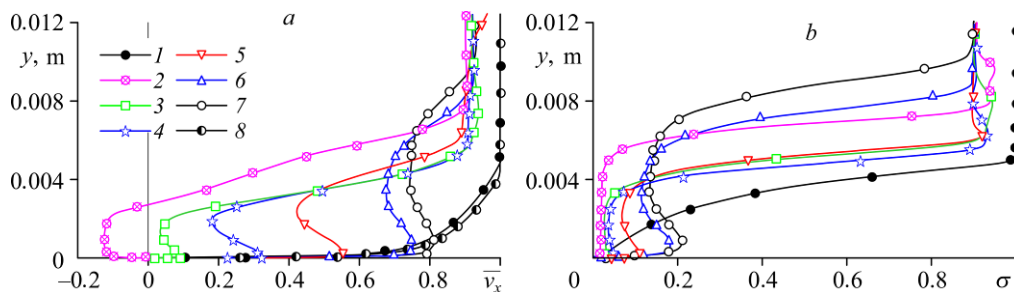

Fig. 5. Velocity and total pressure profiles in the boundary layer.
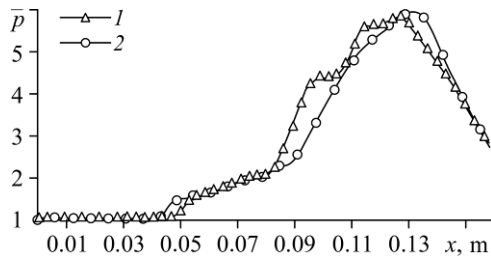$x = 0.04$ m (*1*), 0.085 m (*2*), 0.1 m (*3*), 0.11 m (*4*), 0.13 m (*5*), 0.15 m (*6*), 0.159 m (*7*), and 0 m (*8*).

The further increase in pressure behind the re-attachment region at $x \sim 0.1$ m is associated with flow deceleration in the compression waves and in the reattachment shock *4* (see Fig. 4*b*), while its decrease at $x > 0.12$–0.13 m is caused by the expansion waves *5* from the inflection point of the upper contour of the channel.

The spanwise distributions of pressure on the bottom surface in several characteristic cross sections can be estimated from the data in Fig. 7, where the rib positions are also indicated. The curves show the data in the cross section in the separation region (*1*), in the cross section directly behind the separation region (*2*), near the maximum of pressure along the configuration (*3*) (see Fig. 6), and in the region of the pressure decrease along the configuration (*4*). It can be noted that the pressure distributions are symmetric with respect to the vertical plane of symmetry of the configuration $z = 0$. The pressure peaks, especially in the initial cross sections, correspond to the rip tips, and the pressure levels off further downstream. The character of the pressure distributions near the side walls of the channel in cross sections *3* and *4* is determined by the presence of corner vortices.

The distributions of the relative pressure in the longitudinal sections of the side surface (denoted in Fig. 2*a* as y_1, y_2, and y_3) are shown in Fig. 8. Based on the initial pressure growth, one can estimate the position of the separation region beginning. The end of this region in each section is marked by the reattachment line R, which practically coincides with the local pressure maximums. The character of the pressure distribution has to be correlated with the positions of the sliding shock waves (see Fig. 4*b*) incident onto the side surface. For example, the decrease in pressure along curve *3* in the interval $x \sim 0.095 - 0.105$ m is associated with the expansion fan *5* from the inflection point of the upper contour, and the further increase is caused by the reflected shock *6*. The pressure peak along curve *2* at $x \sim 0.12$ m is caused by the interaction of the reattachment shock *4*, and the subsequent decrease in pressure is due to the expansion fan from the inflection point of the upper contour.

The presence of longitudinal lines of convergence and divergence behind the boundary layer separation region (see Figs. 2 and 3) testifies to possible existence of streamwise vortices
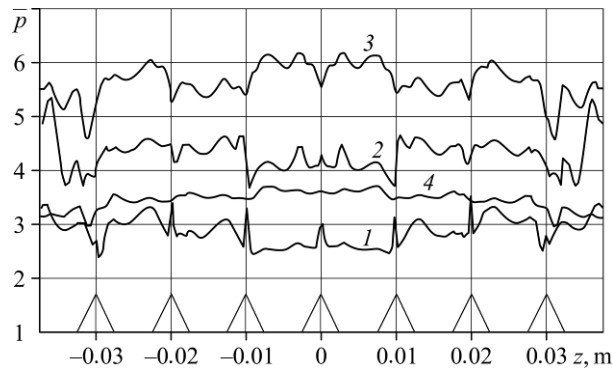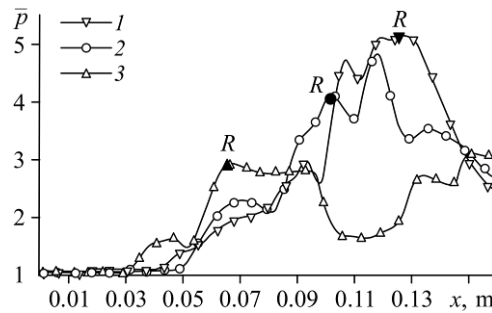

Fig. 7. Distributions of the relative pressure
in the cross sections.
$x = 0.09$ m (*1*), 0.104 m (*2*), 0.13 m (*3*), and 0.15 m (*4*).

Fig. 8. Distributions of the relative pressure
over the side surface.
$\bar{y} = 0.19$ (*1*), 0.43(*2*), and 0.85 (*3*).

between the ribs. Visualization of 3D vortex flows based on the results of numerical simulations is a complex problem [19, 20]. The most popular methods are the construction of lines of equal values of parameters (isolines), streamlines, and velocity vector fields.

   Figure 9 represents the flow field in the form of the Mach number contours in the characteristic cross sections of the channel with indication of the levels in some regions. The Mach number contours in these cross sections have to be correlated with the flow in the longitudinal sections shown in Fig. 4. The flow directly ahead of the boundary layer separation region is presented in Fig. 9*a,* which shows the region of the freestream flow with M = 4 and the region behind the shock wave *1* from the compression wedge of the intake with the Mach number M = 3.3 behind it. This shock wave induced the boundary layer separation on the side surface. The separation region boundaries S and R are determined from the data in Fig. 2*a*. The figure also shows the streamlines in the cross section based on the velocity components V_z and V_y. They can be interpreted as a "wake" of 3D streamlines, and they provide an idea about the flow direction and flow swirling. In particular, it is seen that the incoming flow is directed upward from the bottom surface, i.e., it has a velocity component $V_y > 0$ induced by the displacing effect of the boundary layer.

   The cross section $x = 0.104$ m (Fig. 9*b*) is located directly behind the flow separation region. Here one can see the position of the reflected shock wave *2′* followed by the region of flow expansion above the separation region. As it was assumed earlier, there are longitudinal vortex structures in the valleys between the ribs. It is worth noting that they are "symmetric" with respect to the vertical plane of symmetry of the configuration $z = 0$. Namely, there are vortex structures with different directions of rotation on the right and left of this plane. Moreover, there are also vortices at the corners of the configuration between its bottom and side surfaces. These vortices rotate in the opposite direction as compared to the vortices between the ribs.

   The cross section $x = 0.13$ m (Fig. 9*c*) is located at a considerable distance from the separation region. Based on the Mach number contours, one can see the shock wave reflected from the upper wall of the channel *6* and the reattachment shock *4*. The convergence of the streamlines in the region of this shock testifies to a change in the flow direction. Thus, the velocity component behind the shock is $V_y > 0$, i.e., the flow is directed upward from the bottom surface, which is also seen from the streamlines in Fig. 4*b*. Initially, ahead of the shock wave *4,* the flow behind the separation region is directed toward the bottom surface of the channel. A pair of counterrotating vortices is formed in the region between the ribs. Later on, this configuration of the vortex system apparently fails. Thus, further downstream, in the cross section $x = 0.159$ m (Fig. 9*d*), there are no vortices between the ribs, and only vortices in the lower corners of the intake channel are visible. In this cross section, one can see the position of the shock wave *6′*, which is a "continuation" of the shock wave *6* after its interaction with the reattachment shock *4*. The figure shows the upper boundary of the boundary layer domain *8* behind the separation region, which is also noted in Fig. 4*b* and is consistent with the velocity profiles (see Fig. 5, curve *7*).
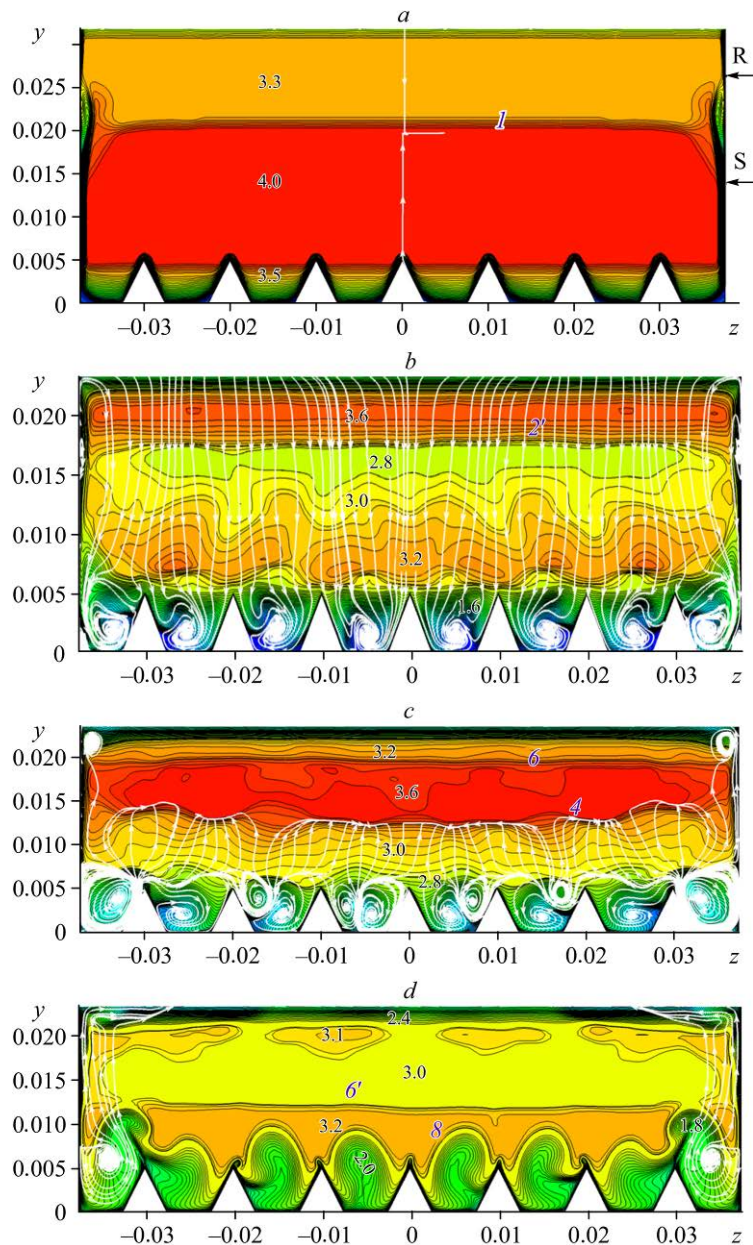
Fig. 9. Flow field in configuration cross sections.
$x = 0.046$ m (*a*), 0.104 m (*b*), 0.13 m (*c*), and 0.159 m (*d*).

Conclusions

A three-dimensional flow with shock wave incidence onto a longitudinally-ribbed surface in a channel with a rectangular cross section was numerically simulated. The data were obtained for the Mach number M = 4 by means of solving the Reynolds-averaged Navier–Stokes equations with the k-ω SST turbulence model. The channel flow structure was studied. The distributions of the limiting streamlines on the surface, Mach number contours in the channel cross sections, and profiles of velocity and total pressure in the boundary layer were presented.

It was shown shock wave-boundary layer interaction on a longitudinally-ribbed surface leads to flow separation with swept streamlines both on the ribs and in the valleys between

the ribs. In this case, flow separation occurs earlier as compared to the corresponding data for the flow in a model intake with a flat bottom surface [16]. Longitudinal vortex structures are formed in the valleys between the ribs behind the boundary layer separation region. The presence of these structures is demonstrated by the distributions of the transverse flow streamlines in the channel cross sections. Both the distributions of the limiting streamlines on the longitudinally-ribbed bottom surface and the positions of the streamwise vortex structures are symmetric with respect to the vertical plane of symmetry of the configuration as a whole. In particular, vortex structures with different directions of rotation are observed on the right and left of this plane.

References

1. **J. Seddon and E. Goldsmith,** Intake aerodynamics, AIAA Education Ser., Reston, 1985.

2. **D.M. van Wie,** Scramjet intakes, in: Scramjet Propulsion, E.T. Curran and S.N.B. Murthy (Eds.), Progress in Astronautics and Aeronautics, 2000, Vol. 189, P. 447–511.

3. **Yu.P. Gounko and I.I. Mazhul,** Gas-dynamic design of a two-dimensional supersonic inlet with the increased flow rate factor, Thermophysics and Aeromechanics, 2012, Vol. 19, No. 4, P. 363–379.

4. **F. Falempin, M.A. Goldfeld, Yu.V. Semenova, A.V. Starov, and K.Yu. Timofeev,** Experimental study of different control methods for hypersonic air inlets, Thermophys. Aeromech., 2008, Vol. 15, No. 1, P. 1–9.

5. **M.A. Goldfeld,** Effect of flow velocity on inlet compression surfaces on the efficiency of boundary layer bleeding, Sib. Fiz. Zh., 2019, Vol. 14, No. 3, P. 15–25.

6. **V.V. Zatoloka and G.A. Kisel,** Swept surface boundary layer bleeding in a hypersonic convergent inlet, Fiz. Gazodinamika (Aerofiz. Issled. No. 6), ITAM SB RAS, Novosibirsk, 1976, P. 61– 62.

7. **Yu.P. Gounko, I.I. Mazhul, and A.M. Kharitonov,** Aerodynamic design and experimental modeling of an innovative supersonic three-dimensional air-intake, The Aeronautical J., 2013, Vol. 117, No. 1192, P 559 –584.

8. **Yu.P. Gounko and I.I. Mazhul,** Experimental characteristics of a supersonic three-dimensional air inlet with adjustable throaty, Thermophysics and Aeromechanics, 2013, Vol. 20, No. 1, P. 49 – 64.

9. **Yu.P. Gounko,** Supersonic inlet (with multislotted bleeding), Patent No. 2672825 RF, MPK[51]F02C 7/04, B64D 33/02, SPK[52]F02C 7/04, F64D 33/02, patent holder ITAM SB RAS, No. 2017113272; appl. 17.04.2017; publ. 19.10.2018, Bul. No. 32; priority 17.04.2917.

10. **Yu.A. Litvinenko, V.G. Chernoray, V.V. Kozlov, L.L. Lefdal, G.R. Grek, and H. Chun,** Effect of riblets on the development of the Λ-structure and its transformation to a turbulent spot, Dokl. Akad. Nauk, 2006, Vol. 407, No. 2, P. 194 –197.

11. **I.D. Zverkov and B.Yu. Zanin,** Wing form effect on flow separation, Thermophysics and Aeromechanics, 2003, Vol. 10, No. 2, P. 197–204.

12. **V.V. Bogolepov, V.N. Brazhko, L.V. Dozorova, G.I. Maikapar, and V.Yu. Neiland,** Aerodynamic heating of wavy surfaces in a supersonic turbulent boundary layer, Uch. Zap. TsAGI, 1987, Vol. 18, No. 6, P. 1–7.

13. **H.J. Brandon, R.V. Masek, and J.C. Dunavant,** Aerodynamic heating to corrugation stiffened structures in thick turbulent boundary layers, AIAA J., 1975, Vol. 13, No. 11, P. 1460 –1466.

14. **Fluent 6.3.** User's Guide. Fluent Inc., Lebanon, USA, 2006.

15. **A.A. Zheltovodov and D.D. Knight,** Ideal-gas shock wave-turbulent boundary-layer interactions in supersonic flow and their modeling: three-dimensional interactions, in: Shock Wave-Boundary-Layer Interactions, H. Babinsky and J. Harvey (Ed.), 2011, P. 202–258.

16. **I.I. Mazhul,** Supersonic flow in the rectangular duct of an air inlet with the separation-induced interaction of the boundary layer with shock waves, Thermophysics and Aeromechanics, 2020, Vol. 27, No. 4, P. 507–518.

17. **V.I. Kornilov,** Three-Dimensional Near-Wall Turbulent Flows in Corner Configurations, SB RAS, Novosibirsk, 2013.

18. **V.I. Kornilov,** Correlation of the separation region length in shock wave/channel boundary layer interaction, Experiments in Fluids, 1997, No. 23, P. 489 – 497.

19. **Visualization** of Data of Physical and Mathematical Modeling in Gas Dynamics, V.N. Emel'yanov and K.N. Volkov (Eds.), Fizmatlit, Moscow, 2018.

20. **K.N. Volkov,** Methods of vortex flow visualization in computational fluid dynamics and their application in solving applied problems, Nauch.-Tekhn. Vest. Inform. Tekhnol., Mekh. Opt., 2014, No. 3 (91), P. 1–10.